J Porous Mater
DOI 10.1007/s10934-016-0145-8

Preparation of Mg–Zn bimetallic doped Na-containing bioceramic from sodium metasilicate

Enobong R. Essien[1,2] · **Luqman A. Adams**[2]

Abstract Glass–ceramic materials in the composition (mol%) 23.5 Na_2O–23.5CaO–xMgO–xZnO–47SiO_2–(6-2x) P_2O_5 ($x = 0$ and 1.5) were prepared by the sol–gel technique using sodium metasilicate (Na_2SiO_3) as source of Na_2O and SiO_2. Bioactivity was investigated in vitro by examining apatite formation on the surface of the samples after treatment in acellular simulated body fluid (SBF). Formation of bioactive apatite layer on the samples was confirmed by using scanning electron microscope, X-ray diffraction and Fourier transform infrared spectroscopy. Reactivity of the materials in SBF was based on changes in pH and ionic concentration of the solution as a function of immersion duration. Results obtained indicated that the sample doped with Mg and Zn exhibited greater crystallinity containing phases such as $CaMgSi_2O_6$, $Ca_2MgSi_2O_7$, $CaSiO_3$, $Na_2CaSi_3O_9$, $Na_2CaSi_3O_8$, $CaZnSi_2O_7$ and a new secondary phase, clinohedrite ($CaZnSiO_4{\cdot}H_2O$), while the undoped sample contained a single crystalline phase composed of $Na_2Ca_2Si_3O_9$. After 7 days in SBF, phase transformation occurred at different rates on the materials leading to formation of apatite layer. The result shows that controlled amounts of MgO and ZnO may be useful in tuning up the mechanical properties of bioactive glasses while maintaining bioactivity.

Keywords Sol–gel process · Sodium metasilicate · Magnesium · Zinc · Bioceramics

✉ Enobong R. Essien
reggiessien@gmail.com

[1] Department of Chemical Sciences, Bells University of Technology, KM 7 Idiroko Road, P.M.B, 1015 Ota, Nigeria

[2] Department of Chemistry, University of Lagos, Lagos, Nigeria

1 Introduction

Bioactive glasses and ceramics have been extensively studied since the pioneering work of Hench et al. [1] with 45S5 bioactive glass. Interest in these materials derives from their ability to form direct chemical bonds to living bone tissue under physiological conditions [2]. Thus they have been widely applied as implants in the healing of bone defects arising from osteoporosis, tumour removal, spinal fusion [3] as well as in drug delivery, tissue engineering scaffolding and cell cultivation [4–6]. 45S5 bioactive glass has the composition SiO_2–Na_2O–CaO–P_2O_5, but presently various types of bioactive glasses have been developed to further enhance biological responses during application.

Magnesium as a trace element has been shown to play important role in bone development and maintenance [7, 8]. Apatite where Mg was substituted for Ca demonstrated excellent biocompatibility and great osteoconductive behaviour over time [9, 10]. Zinc is known for its anti-inflammatory effect and activation of protein synthesis in osteoblast, causing stimulation of in vitro bone formation [11]. Furthermore, Zn activates ATPase enzyme and indirectly controls differentiation to osteoblast cells [12].

These benefits of zinc have inspired the development of zinc-containing ceramics for bone engineering applications. Calcium silicate ceramics such as $Ca_2ZnSi_2O_7$ have recently been found to support human osteoblast-like cells attachment to a well-organized cytoskeleton structure. In addition, they support an increased cellular proliferation and differentiation with increased expression levels of osteoblast-related mRNAs (alkaline phosphatase, collagen type I, osteocalcin) when compared to calcium silicate ($CaSiO_3$) ceramics [13, 14]. Consequently, some authors [15–18] reported the stimulation of bone formation from zinc modified calcium phosphate ceramics applied in vivo.

Published online: 16 February 2016

Preparation of bioactive glass ceramics substituted with magnesium and zinc and the resultant delay effects of these glasses on apatite formation is well documented [12, 19–21]. However, in these studies sodium was not included in the composition. An important advantage of Na in sol–gel bioactive glasses is that it could lead to higher dissolution rates of the final materials in aqueous media, which is an important factor for the interaction of the material with living tissues [6, 22]. In this work, we studied the bioactivity of sodium-based glass co-doped with Mg and Zn in simulated body fluid. We chose Na_2SiO_3 instead of tetraethyl orthosilicate (TEOS), often used in sol–gel-derived glasses, as silica source, for the dual purpose of adding Na and reducing cost [23].

2 Materials and methods

2.1 Materials

The chemicals for the preparation of the bioactive glass included: sodium metasilicate (Na_2SiO_3, weight ratio $SiO_2/Na_2O = 2.0 \pm 0.05$; Shuanglian Fine Chemical Co.), nitric acid (HNO_3; Fluka), phosphoric acid (H_3PO_4; BDH Laboratory), calcium nitrate tetrahydrate ($Ca(NO_3)_2{\cdot}4H_2O$; LOBA), magnesium nitrate hexahydrate ($Mg(NO_3)_2{\cdot}6H_2O$; Sigma-Aldrich) and zinc nitrate hexahydrate ($Zn(NO_3)_2{\cdot}6H_2O$; Sigma-Aldrich). All chemicals where used as obtained without further purification.

2.2 Synthesis of glass samples

Glass–ceramics in the compositional range (mol%) 23.5 Na_2O–23.5CaO–xMgO–xZnO–47SiO_2–(6-2x)P_2O_5 glass, where $x = 0$ and 1.5 (Table 1), were prepared by the sol–gel method. The gel was synthesized by hydrolysis and polycondensation of stoichiometric amounts of Na_2SiO_3, H_3PO_4, $Ca(NO_3)_2{\cdot}4H_2O$, $Mg(NO_3)_2{\cdot}6H_2O$ and $Zn(NO_3)_2{\cdot}6H_2O$ in the presence of deionized water (molar ratio 10 H_2O/(total mole of reagents used)). 0.1 M HNO_3 was used as catalyst. Briefly, the Na_2SiO_3 was mixed with deionized water and HNO_3 using a magnetic stirrer, then H_3PO_4, $Ca(NO_3)_2{\cdot}4H_2O$, $Mg(NO_3)_2{\cdot}6H_2O$ and $Zn(NO_3)_2{\cdot}6H_2O$ were successively added slowly by keeping 1 h intervals between additions. After mixing all reagents, the solution was introduced into sealed polyethylene containers serving as mould and labelled BG for the undoped sample and BG-Mg/Zn for the sample doped with Mg and Zn. Afterwards, the samples were allowed to gel at room temperature for 72 h and aged at 60 °C for 72 h. The drying process was carried out at 130 °C for 42 h, followed by heating at 700 °C for 2 h Finally, the samples were treated at 950 °C for 2 h, using a heating rate of 10 °C/min to obtain glass–ceramic [24]. A flowchart of the process is given in Fig. 1.

Table 1 Composition of the glass–ceramic samples

Sample	Composition (mol%)					
	Na_2O	CaO	MgO	ZnO	SiO_2	P_2O_5
BG	23.5	23.5	0	0	47	6
BG-Mg/Zn	23.5	23.5	1.5	1.5	47	3

2.3 Characterization

The compressive strength of the sintered samples were measured using a Testometric OL11 INR (Lancashire, England) mechanical tester at crosshead speed of 0.5 mm/min. The samples were cylindrical in shape with dimensions 12 mm × 24 mm (diameter × height). During the compression test, the load was applied until densification commenced. The compression strength was determined using the relation:

$$\sigma_c = F/\pi r^2 \quad (1)$$

where σ_c is the compressive strength, F is the applied load at failure and r is the sample radius.

The microstructure and pore dimension of the samples was characterized in a EVO/MAIO scanning electron microscope (SEM). The samples were carbon-coated and observed at an accelerating voltage of 15 kV.

X-ray diffraction (XRD) analysis after sintering and after each immersion experiment in SBF was used to investigate the type of phases present in the materials. The samples were first ground to powder, then 0.1 g of powder was measured in a PANalytical Empyrean X-ray diffractometer using CuKα radiation source of wavelength (λ) = 0.154056 nm operated at 40 kV and 40 mA to obtain the diffraction patterns in the 2θ range from 5° to 90°.

Fourier transform infrared spectroscopy (FTIR) (Bruker-Alpha, Platimum ATR) with wavenumber range of 4000–500 cm^{-1} was used to monitor the nature of bonds present in the glass network and to confirm apatite formation on the surface of the samples.

2.4 In vitro bioactivity test in simulated body fluid

In vitro tests were performed by soaking samples in SBF (pH 7.4) at 36.5 °C according to the standard procedure proposed by Kokubo et al. [25] using analytical grade reagents: NaCl, $NaHCO_3$, KCl, $K_2HPO_4{\cdot}3H_2O$, $MgCl_2{\cdot}6H_2O$, $CaCl_2$, trishydroxymethyl aminomethane [Tris-buffer, $(CH_2OH)_3CNH_2$], and 1 M HCl containing a similar ionic concentration as found in human blood plasma (Table 2). Samples immersed in SBF solution in clean

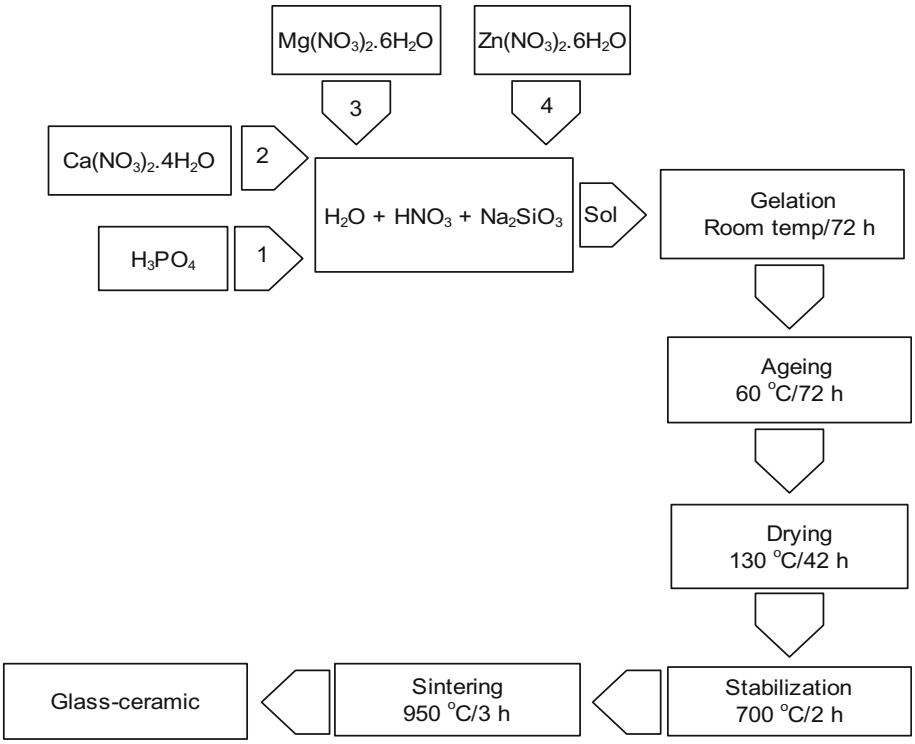

Fig. 1 Flowchart for the preparation of the samples using the sol–gel method. Formation of BG does not involve steps 3 and 4

sterilized plastic bottles at a concentration of 0.01 g/ml were placed in an incubator for a maximum of 7 days. The SBF solution was not refreshed during the duration of the experiment to enable the monitoring of pH and changes in concentration. Once withdrawn from the SBF, samples were rinsed with deionized water and left to dry at ambient temperature in a desiccator for 7 days. Formation of apatite layer on the glass surface was evaluated by SEM, XRD and FTIR as described above. The SBF was analyzed after immersion periods of 1, 3 and 7 days to evaluate changes in concentration of Na, Ca, Si, Mg, Zn and P. Atomic absorption spectrophotometer (AAS) (Perkin Elmer, Buck A Analyst) was employed to examine Na, Ca, Si, Mg and Zn, while P was estimated by UV visible light spectrophotometer (Uniscope, SM 7504) using colorimetric assay [26].

3 Results and discussion

3.1 Mechanical properties

Figure 2 shows the compressive strength of the specimens BG and BG-Mg/Zn after heat treatment at 950 °C for 3 h. The compressive strength of the sample before doping (BG) is 5.67 ± 5 % Mpa but increased significantly to 8.86 ± 5 % Mpa when 3 mol% of the P_2O_5 was replaced with 1.5 mol% each of Mg and Zn (BG-Mg/Zn). BG shows a complete collapse as a maximum stress is reached but BG-Mg/Zn continues to bear more load beyond its maximum stress limit until it finally collapses. This can be attributed to densification of pores which caused the curve to rise again [27], thus suggesting that pore struts in BG-Mg/Zn may be thicker than those in than BG.

3.2 Morphology

The SEM micrographs of the samples after sintering at 950 °C are shown in Fig. 3. As observed, both samples BG and BG-Mg/Zn contain homogeneous surfaces with a few voids, Fig. 3a, b respectively. However, the surface of the doped sample (BG-Mg/Zn) appears more agglomerated and crystalline with thicker pore struts (Fig. 3b). This thick pore struts were earlier suggested as being responsible for the enhanced mechanical performance of BG-Mg/Zn. After immersion in SBF for 7 days, appreciable changes in morphology can be seen (Fig. 4). The surface of the BG sample becomes constituted by growth of spherical

Table 2 Ion concentrations (mM) in human plasma in comparison with SBF

Ion	Na^+	K^+	Mg^{2+}	Ca^{2+}	Cl^-	HCO_3^-	HPO_4^{2-}	SO_4^{2-}
SBF	142.0	5.0	1.5	2.5	147.8	4.2	1.0	0.5
Human plasma	142.0	5.0	1.5	2.5	103.0	27.0	1.0	0.5

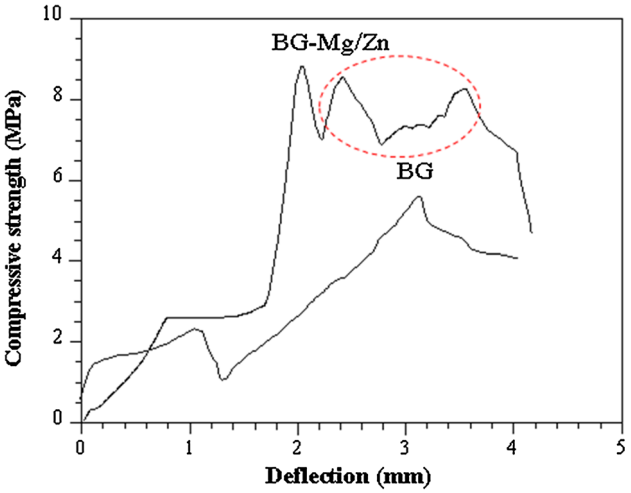

Fig. 2 A curve of compressive strength against deflection for BG and BG-MgZn samples. The *dotted* region shows densification of pore struts

particles (Fig. 4a). The same effect is observed in the micrograph of BG-Mg/Zn, Fig. 4b, which, in addition appears coarser. These changes may be attributed to the formation of apatite as a result of surface reactions occurring between the materials and SBF [28].

The average pore diameter of BG after sintering was 2.82 μm as shown in Fig. 5a. By contrast, BG-Mg/Zn exhibited smaller average pore diameter of 1.47 μm (Fig. 5b), while the corresponding pore area for BG was 0.41 μm^2 (Fig. 5c), and 0.21 μm^2 for BG-Mg/Zn (Fig. 5d). The microstructure and porosity presented by these materials are important requirements for enhanced cell adhesion, vascularization, infiltration, and osteointegration on the materials [29–34].

3.3 Phase evaluation

Figure 6 shows the diffraction patterns of the two samples, BG and BG-Mg/Zn. The XRD spectrum of BG is characterized by peaks with low intensity identified as crystals of $Na_2Ca_2Si_3O_9$ according to the standard PDF No. 22-1455. The mechanical strength of Na–containing glasses has been attributed to the presence of $Na_2Ca_2Si_3O_9$ crystalline phase [27, 28, 35]. The XRD patterns of the BG-Mg/Zn is considerably different compared with BG in terms of intensity and number of phases present. The crystalline phases identified include diopside ($CaMgSi_2O_6$) [36], wollastonite ($CaSiO_3$) [37], akermanite ($Ca_2MgSi_2O_7$) [38], sodium calcium silicates ($Na_2CaSi_3O_9$) PDF No. 45-0550 and ($Na_2CaSi_3O_8$), PDF No. 12-0684, and calcium zinc silicate ($CaZnSi_2O_7$) [39]. In addition, a new secondary phase clinohedrite, $CaZnSiO_4{\cdot}H_2O$ [40] was identified in the BG-Mg/Zn sample.

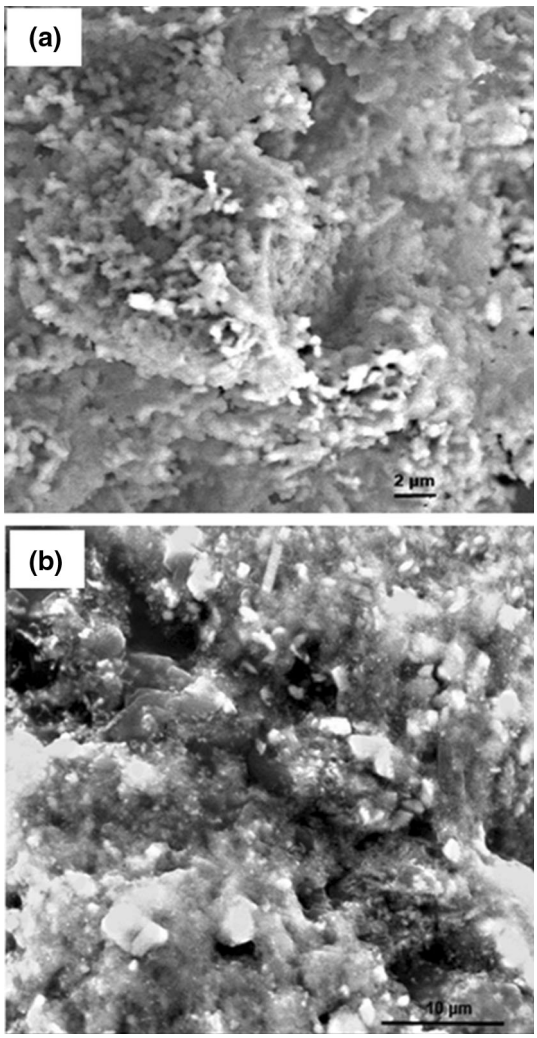

Fig. 3 SEM micrographs of BG (**a**) and BG-Mg/Zn (**b**) showing homogeneous surfaces

The presence of these phases accounted for the crystalline nature of the BG-Mg/Zn, as was observed earlier in the SEM micrograph (Fig. 3b). The presence of sharp peaks with high intensity supports the finding that addition of MgO or ZnO could widen the sintering window and increase the activation energy for crystallization [41–44]. The BG-Mg/Zn sample almost attained full crystallization when heated to 950 °C for 3 h, which was important for improving mechanical properties.

The XRD spectra of the samples after soaking in SBF for 7 days are presented in Fig. 7. BG completely transformed to amorphous phase, while the only peaks observed are those recognized as hydroxyapatite (HA) [45]. The spectrum of BG-Mg/Zn after soaking for the same period is markedly different. Most of the sharp peaks initially seen in the parent sample, are still very visible, although present at low intensity. In addition, some HA peaks [45] emerged in the spectrum. This result agrees with previous reports

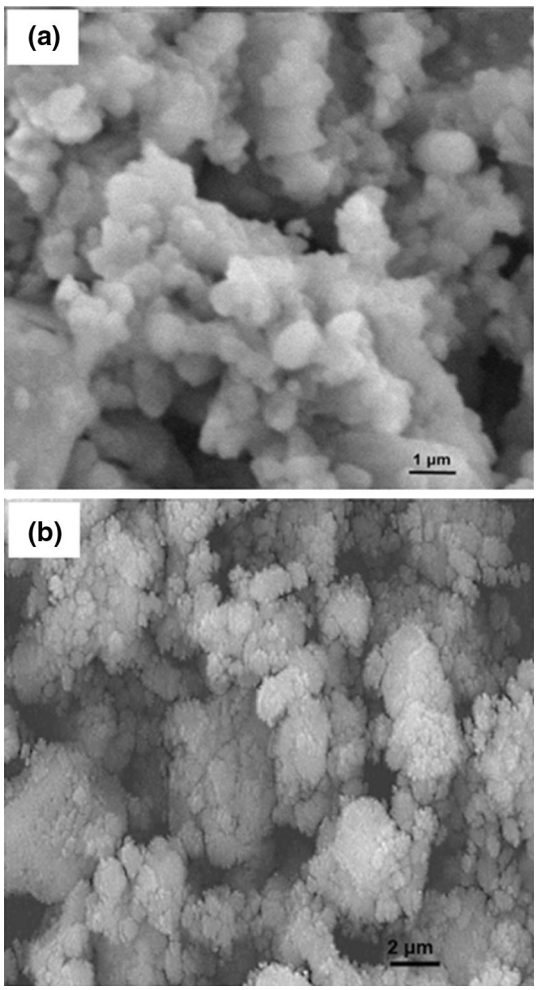

Fig. 4 SEM micrographs of BG (**a**) and **b** BG-Mg/Zn after soaking in SBF of 7 days showing the growth of apatite

that inclusion of MgO and ZnO decreases bioactivity as stated earlier. One way of explaining this phenomenon is that in the undoped material (BG) the single crystalline phase ($Na_2Ca_2Si_3O_9$) formed has high dissolution rate in SBF due to the presence of soluble Na^+ ions, then transforms to amorphous calcium phosphate phase of HA by incorporating Ca^{2+} from the solution [1]. In the case of BG-Mg/Zn, the presence of several crystalline phases formed from Mg^{2+} and Zn^{2+} ions decreased its overall dissolution kinetics in SBF. Consequently, most of the crystalline phases were only partly soluble after 7 days in SBF solution. Based on previous studies [46, 47], apatite nucleation on BG-Mg/Zn may be ascribed to the presence of the $CaMgSi_2O_6$ and $Ca_2MgSi_2O_7$ crystalline phases.

3.4 Reactivity in SBF

The reactivity of the samples monitored by pH changes as a function of immersion time in SBF is shown in Fig. 8. There is a sharp increase in pH during the first 2 days, which shows the ability of the materials to exchange alkali and alkaline earth ions (Na^+, Ca^{2+} or Mg^{2+} and Zn^{2+}) rapidly with H^+ or H_3O^+ ions in the SBF solution. With increase in immersion time, the increase in pH becomes gradual. The fast change in the pH is due to the time dependent and kinetic nature of the interaction between the fluid and sample surface.

The release of Ca^{2+} and other ions resulting in pH increment can be explained by the mechanism proposed by Kokubo et al. [48] for the formation of an apatite-like layer on materials containing SiO_2 and CaO. As hydroxy-carbonated (HCA) layer is progressively crystallized from the amorphous $CaO–P_2O_5$ film deposited on the surface, the free surface available on the material for further leaching of Ca^{2+} ions reduces. This results in a slower increase in the pH of the fluid as evidenced in the data depicted in Fig. 8. Furthermore, the pH of BG-Mg/Zn increases slightly more than that of BG, attributed to the joint contribution of additional Mg^{2+} and Zn^{2+} ions leached into the SBF solution from the BG-Mg/Zn glass surface.

Ion release leading to changes in pH from the initial value of 7.4 culminating in 9.0 for BG and 9.3 for BG-Mg/Zn can be supported by the result of analysis of the SBF solution for 1, 3 and 7 days which is shown in Table 3. The fast release of Na from both samples throughout the period of immersion explains the sharp increase in pH. There is also a fast release of Ca during the first day of immersion of both samples in SBF, thereafter the concentration decreases gradually after the first 2 days due to uptake by the samples to form HA which caused a slow rise in pH as observed earlier. The formation of HA is further supported by the gradual decline in the concentration of P as immersion days increase, suggesting withdrawal to form apatite on the sample surfaces. For sample BG, as expected, the concentration of Mg in the SBF solution remained almost constant throughout the period of immersion since no Mg was originally included in the sample. Mg and Zn releases for sample BG-Mg/Zn are rather slow but sufficient to increase the pH of the solution by 3 units higher than BG.

An interesting phenomenon is also observed with the change in concentration of Si in the SBF solution during the periods of study. The release rate of Si in BG is higher than BG-Mg/Zn, which also indicates that BG has a higher degree of degradation than BG-Mg/Zn in SBF.

3.5 Assessment of bonds and confirmation of apatite

Figure 9 shows the FTIR spectra of the samples before immersion in SBF. Several peaks are observed near 1013, 908, 732, 626, 576 and 527 cm^{-1} in BG. The sharp peak at 1013 cm^{-1} corresponds to Si–O–Si(s, asym) asymmetric stretching mode, the one at 732 cm^{-1} is associated with symmetric stretching vibration of Si–O–Si(s, sym) [49].

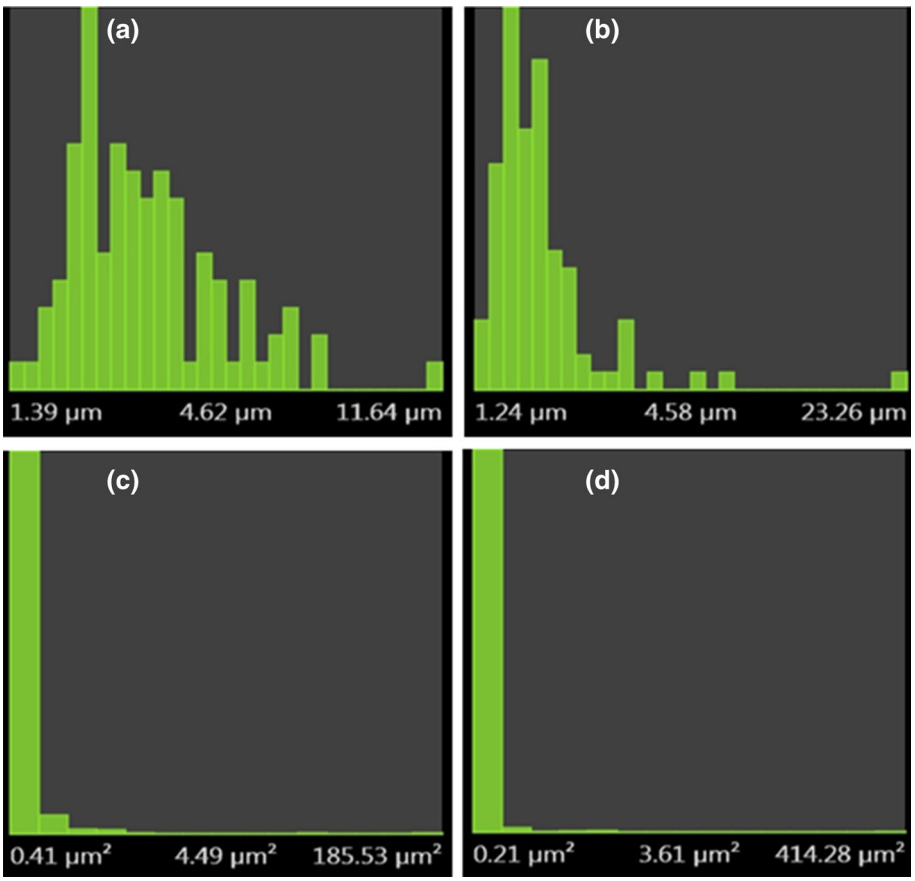

Fig. 5 Histogram showing the pore diameter of **a** BG, **b** BG-Mg/Zn as well as pore area of **c** BG and **d** BG-Mg/Zn as determined by fibrematrics using SEM machine

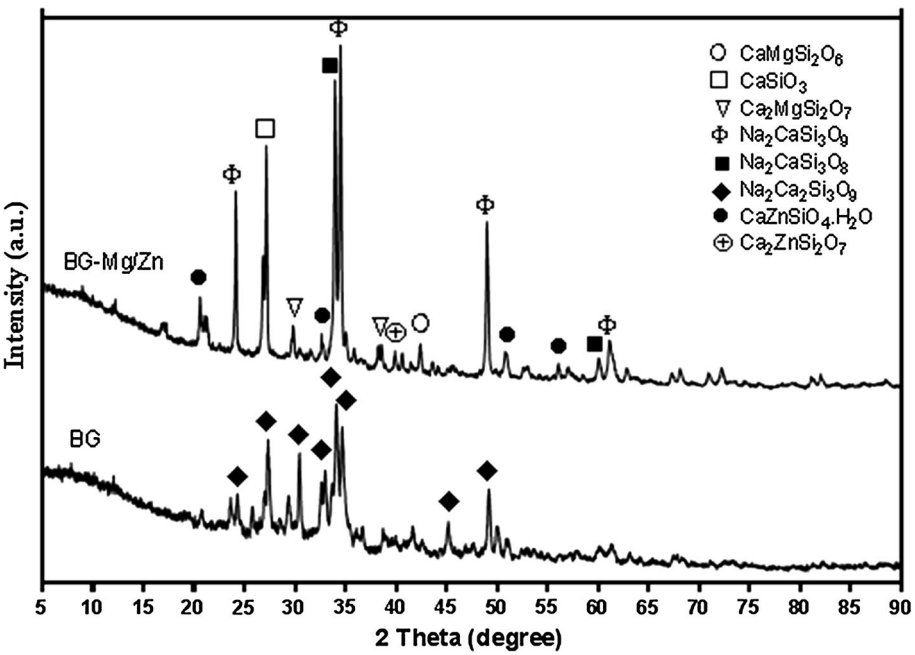

Fig. 6 Diffraction patterns of BG and BG-Mg/Zn samples after sintering showing the presence of different bioactive crystalline phases

Also, the peak at 950 cm^{-1} is related to ($Si–O^{-}$) of SiO_4^{4-} tetrahedra having two non-bonding oxygen per tetrahedron (Si–O–2NBO) [50], resulting from the presence of network modifying cations. Furthermore, the peaks at 626, 576 and 527 cm^{-1} are related to P–O deformation modes in crystalline phosphate [50]. Additional bands are observed at

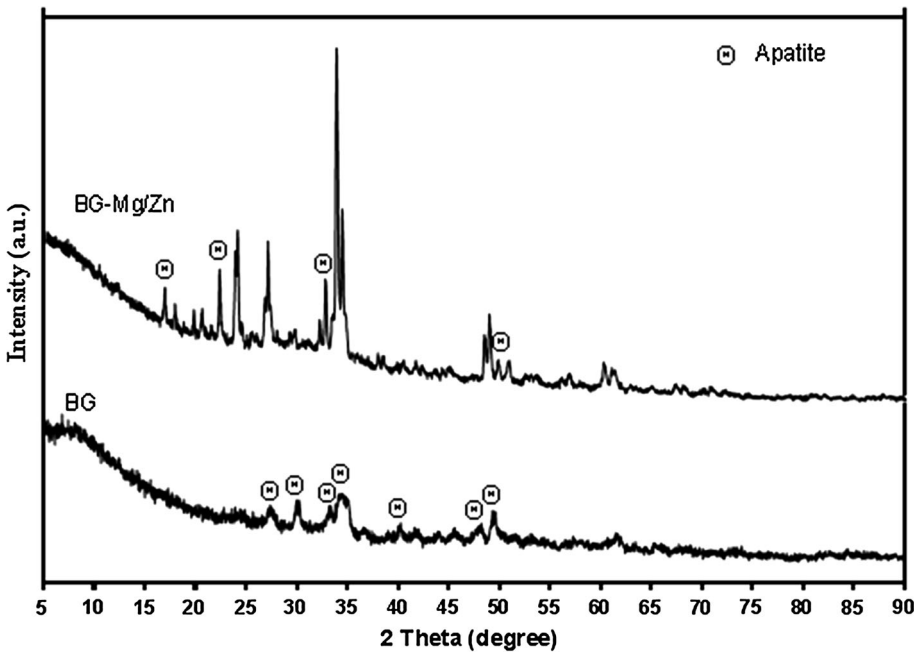

Fig. 7 XRD spectrum of BG and BG-Mg/Zn after immersion in SBF for 7 days showing growth of apatite

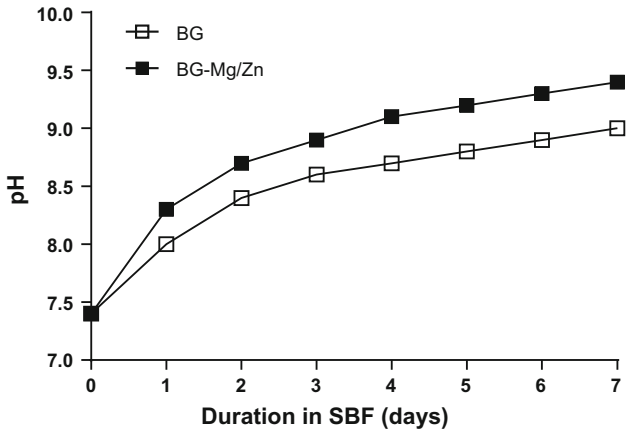

Fig. 8 pH changes of BG and BG-Mg/Zn samples in SBF for 7 days

3237, 1650 and 1444 cm^{-1} in the spectrum of the BG-Mg/Zn sample. The broad band centred at 3237 cm^{-1} is attributed to O–H stretching vibration of water, which is further confirmed by weak water adsorption band around 1650 cm^{-1}. This may be related to the presence of clinohedrite ($CaZnSiO_4 \cdot H_2O$) identified in the XRD result (Fig. 6). The peak at 1444 cm^{-1} is due to the presence of ionic surface carbonates [51] in the sample due to adsorption of atmospheric CO_2 during the sol preparation by labile surfaces formed by the additional alkaline earth metal cations Mg^{2+} and Zn^{2+}. It is particularly noted that the small phosphate peak near 576 cm^{-1} seen in BG is absent in the spectrum of BG-Mg/Zn. This can be explained from the fact that the substitution of MgO and ZnO decreased the total concentration of P_2O_5 in the BG-Mg/Zn sample.

Table 3 Ionic concentration of the elements after various immersion periods in SBF

Samples	Concentration (ppm) of SBF after soaking times			
	0 day	1 day	3 days	7 days
BG				
Na	3266	3297.74	3317.32	3331.64
Ca	100	121.91	119.42	86.65
Si	0	16.06	22.48	30.13
Mg	36	35.38	35.14	35.08
Zn	0	0	0	0
P	31	28.51	24.33	19.81
BG-Mg/Zn				
Na	3266	3281.11	3309.69	3327.22
Ca	100	118.17	113.66	95.83
Si	0	11.20	14.10	19.35
Mg	36	37.75	38.12	39.41
Zn	0	0.48	0.51	0.59
P	31	29.21	27.57	24.90

The FTIR spectra of samples after immersion in SBF for 7 days are presented in Fig. 10. In BG, the peak at 561 cm^{-1} is considered for P–O bending mode in apatite. The bands located at 1392 and 871 cm^{-1} signify the incorporation of carbonate anions from the SBF into the apatite crystal lattice. In the FTIR spectrum of BG-Mg/Zn, the carbonate band at 1444 cm^{-1} decreased in intensity, while there is absence of an absorption band near

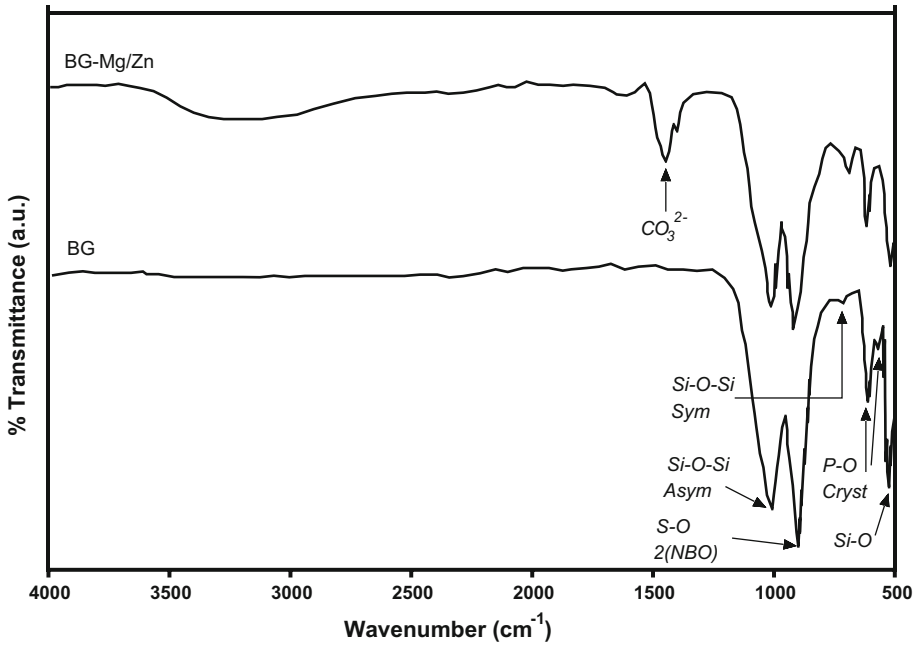

Fig. 9 FTIR spectrum of the samples before immersion in SBF showing the type of bonds present

870 cm^{-1}, confirming that its presence in the spectrum of the sample before soaking in SBF (Fig. 9) was not due to apatite formation. However, a small phosphate peak ascribed to apatite is seen at 577 cm^{-1}.

The FTIR result in Fig. 10 can also be used to advance the speculation given earlier concerning the dissolution behaviour of both samples in SBF that resulted in the diffraction patterns observed in Fig. 7. The Si–O–NBO stretching vibration at 908 cm^{-1} disappears after soaking the BG glass for 7 days in SBF. This shows that leaching of the network modifying cations into the solution was almost complete. In BG-Mg/Zn, the Si–O–NBO bonds is still visible, signifying that some of the modifier cations in the sample were not fully exchanged with the H^+ or H_3O^+ of the SBF, and this resulted in a lower bioactivity.

4 Conclusions

A bioactive glass–ceramic in the composition (mol%) $23.5Na_2O$–$23.5CaO$–$47SiO_2$–$6P_2O_5$ and $23.5Na_2O$–$23.5CaO$–$1.5MgO$–$1.5ZnO$–$47SiO_2$–$3P_2O_5$ were prepared

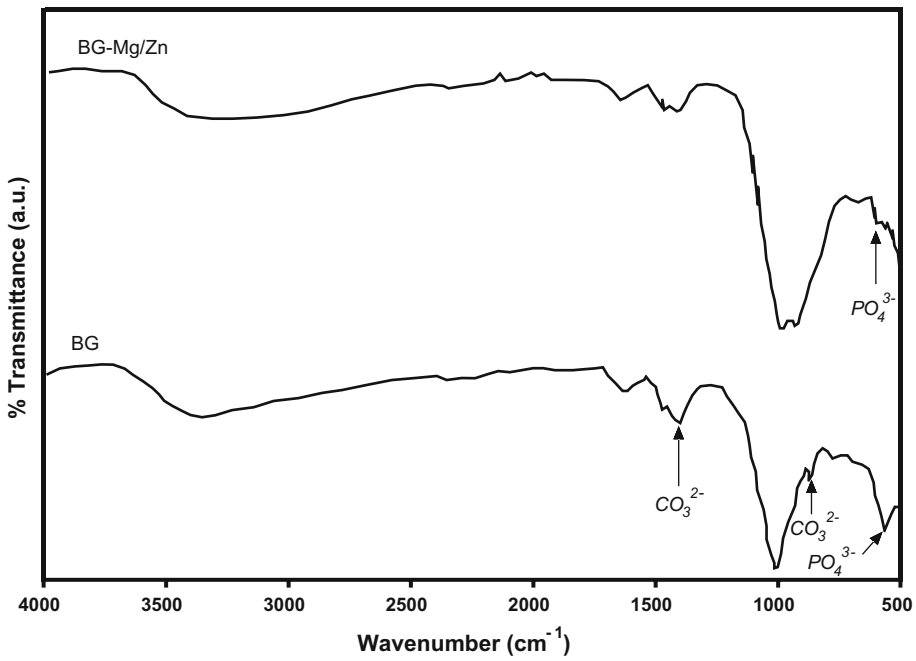

Fig. 10 FTIR spectrum of samples after immersion in SBF for 7 days showing the presence of bonds related to apatite

from sodium metasilicate as precursor to study the bioactivity in SBF of sodium-containing bioactive glass jointly doped with zinc and magnesium. Results obtained showed that multiple crystalline phases were obtained from additions of MgO and ZnO to the quaternary system glass containing sodium. The presence of these phases, although can slow down bioactivity, could have the advantage of contributing to the mechanical strength of a 4-component sodium glass. Interestingly, also, the sodium metasilicate which served as a substitute for TEOS is of low cost. Our study is useful in two folds: first, in contributing to the understanding of the reaction of glasses containing MgO and ZnO in SBF and; second, for economic synthesis of sodalime bioactive glasses co-doped with MgO and ZnO for application in bone tissue repair.

Acknowledgments We are grateful to the management of the Central Teaching and Research Laboratory of Bells University of Technology, Ota, Nigeria, where this research work was conducted. We also thank Mr. Femi Igbari of the College of NanoScience and Technology, Soochow University, China for his assistance with the SEM and XRD characterization.

References

1. L.L. Hench, R.J. Splinter, W.C. Allen, T.K. Greenlee, J. Biomed. Mater. Res. **5**, 117 (1971)
2. X. Yan, X. Huang, C. Yu, H.X. Deng, Y. Wang, Z. Zhang, S. Qiao, G. Lu, D. Zhao, Biomaterials **27**, 3396 (2006)
3. J.R. Jones, Acta Biomater. **9**, 4457 (2013)
4. L.L. Hench, J.M. Polak, Science **295**, 1014 (2002)
5. M. Vallet-Regi, J. Chem. Soc., Dalton Trans. **2**, 97 (2001)
6. M. Vallet-Regi, C.V. Ragel, A.J. Salinas, Eur. J. Inorg. Chem. **2003**, 1029 (2003)
7. J.M. Oliveira, R.N. Correia, M.H. Fernandez, J. Rocha, J. Non-Cryst. Solids **265**, 221 (2000)
8. C.T. Wu, J. Chang, J.Y. Wang, S.Y. Ni, W.Y. Zhai, Biomaterials **26**, 2925 (2005)
9. E. Landi, G. Logroscino, L. Proietti, A. Tampieri, M. Sandri, S. Sprio, J. Mater. Sci. Mater. Med. **19**, 239 (2008)
10. Y.L. Cai, S. Zhang, X.T. Zeng, Y.S. Wang, M. Qian, W.J. Weng, Thin Solid Films **517**, 5351 (2009)
11. M. Yamaguchi, J. Trace Elem. Exp. Med. **11**, 119 (1998)
12. I.S. Kwun, Y.E. Cho, R.A.R. Lomeda, H.I. Shin, J.Y. Choi, Y.H. Kang, J.H. Beattie, Bone **46**, 732 (2010)
13. Y. Ramaswamy, C. Wu, H. Zhou, H. Zreiqat, Acta Biomater. **4**, 1487 (2008)
14. C. Wu, Y. Ramaswamy, J. Chang, J. Woods, Y. Chen, H. Zreiqat, J. Biomed. Mater. Res. B Appl. Biomater. **87**, 346 (2008)
15. A. Ito, K. Ojima, H. Naito, N. Ichinose, T. Tateishi, J. Biomed. Mater. Res. **50**, 178 (2000)
16. Y. Sogo, T. Sakurai, K. Onuma, A. Ito, J. Biomed. Mater. Res. **62**, 457 (2002)
17. A. Ito, H. Kawamura, M. Otsuka, M. Ikeuchi, H. Ohgushi, K. Ishikawa, K. Onuma, N. Kanzaki, Y. Sogo, N. Ichinose, Mater. Sci. Eng., C **22**, 21 (2002)
18. H. Kawamura, A. Ito, T. Muramatsu, S. Miyakawa, N. Ochiai, T. Tateishi, J. Biomed. Mater. Res. A **65**, 468 (2003)
19. A.A. Hamedani, F. Moztarzadeh, D. Bizari, M. Ashuri, M. Tahriri, Key Eng. Mater. **493–494**, 55 (2011)
20. M.R. Majhi, R. Pyare, S.P. Singh, Int. J. Sci. Eng. Res. **2**, 1 (2011)
21. M. Erol, A. Özyuguran, Ö. Çelebican, Chem. Eng. Technol. **33**, 1066 (2010)
22. J.R. Jones, E. Gentleman, J. Polak, Elements **3**, 393 (2007)
23. M. Crisan, M. Raileanu, S. Preda, M. Zaharescu, A.M. Valean, E.J. Popovici, V.S. Teodorescu, V. Matejec, J. Mrazek, J. Optoelectron. Adv. M. **8**, 815 (2006)
24. R.L. Siqueira, O. Peitl, E.D. Zanotto, Mater. Sci. Eng., C **31**, 983 (2011)
25. T. Kokubo, H. Takadama, Biomaterials **15**, 2907 (2006)
26. J.K. Heinonen, R.J. Lahti, Anal. Biochem. **113**, 313 (1981)
27. Q.Z. Chen, I.D. Thompson, A.R. Boccaccini, Biomaterials **27**, 2414 (2006)
28. O. Peitl, E.D. Zanotto, L.L. Hench, J. Non-Cryst, Solids **292**, 115 (2001)
29. K. Rezwan, Q.Z. Chen, J.J. Blaker, A.R. Boccaccini, Biomaterials **27**, 3413 (2006)
30. C. Vitale-Brovarone, M. Miola, C. Balagna, E. Verné, Chem. Eng. J. **137**, 129 (2008)
31. V. Karageorgiou, D. Kaplan, Biomaterials **26**, 5474 (2005)
32. I.O. Smith, F. Ren, M.J. Baumann, E.D. Case, J. Biomed. Mater. Res. B Appl. Biomater. **79**, 185 (2006)
33. J.R. Woodard, A.J. Hilldore, S.K. Lan, C.J. Park, A.W. Morgan, J.A. Eurell, S.G. Clark, M.B. Wheeler, R.D. Jamison, A.J. Wagoner, Johnson. Biomaterials **28**, 45 (2007)
34. C. Vitale-Brovarone, F. Baino, E. Verné, J. Mater. Sci. Mater. Med. **20**, 643 (2009)
35. M.S. Bahniuk, H. Pirayesh, H.D. Singh, J.A. Nychka, L.D. Unsworth, Biointerphases **7**, 41 (2012)
36. P. Richet, B. Mysen, J. Ingrin, Phys. Chem. Miner. **6**, 401 (1998)
37. M.M. Barkley, R.T. Downs, H. Yang, Am. Miner. **96**, 797 (2011)
38. M. Merlini, M. Germmi, G. Cruciani, G. Artioli, Phys. Chem. Miner. **35**, 147 (2008)
39. S.J. Louisnathan, Z. Krstallogr. **130**, 427 (1969)
40. M.A. Simonov, Y.K. Egorov-Tismenko, N.V. Belov, Sov. Phys. Dokl. **2**, 113 (1978)
41. M.J. Brink, Biomed. Mater. Res. **36**, 109 (1997)
42. M. Brink, T. Turunen, R.P. Happonen, A. Yli-Urpo, J. Biomed. Mater. Res. **37**, 114 (1997)
43. E. Vedel, D. Zhang, H. Arstila, L. Hupa, M. Hupa, Glass Technol. Eur. J. Glass Sci. Technol. A **50**, 9 (2009)
44. H. Oudadesse, E. Dietrich, Y.L. Gal, P. Pellen, B. Bureau, A.A. Mostafa, G. Cathelineau, Biomed. Mater. **6**, 035006 (2011)
45. J.M. Hughes, Am. Miner. **100**, 1033 (2015)
46. T. Nonami, S. Tsutsumi, J. Mater. Sci. Mater. Med. **10**, 475 (1999)
47. C.T. Wu, J. Chang, J. Biomed. Mater. Res. B **83**, 153 (2007)
48. C. Ohtsuki, T. Kokubo, T. Yamamuro, J. Non-Cryst. Solids **143**, 84 (1992)
49. V. Aina, G. Malavasi, A.F. Pla, L. Munaron, C. Morterra, Acta Biomater. **5**, 1211 (2009)
50. A.R. Boccaccini, Q. Chen, L. Lefebvre, L. Gremillard, J. Chevalier, Faraday Discuss. **136**, 27 (2007)
51. M. Cerruti, C. Morterra, Langmuir **20**, 6382 (2004)